ISSN 1349-1113
JAXA-RR-07-007E

JAXA Research and Development Report

Effect of Airframe Configuration on Condition of Airflow to Engine in Hypersonic Flow

Takeshi KANDA, Kanenori KATO, Masatoshi KODERA, Kenji KUDO
Atsuo MURAKAMI, Muneo IZUMIKAWA and Shu-ichi WATANABE

December 2007

Japan Aerospace Exploration Agency

Effect of Airframe Configuration on Condition of Airflow to Engine in Hypersonic Flow*

Takeshi KANDA*1, Kanenori KATO*1, Masatoshi KODERA*1, Kenji KUDO*1,
Atsuo MURAKAMI*1, Muneo IZUMIKAWA*1, and Shu-ichi WATANABE*2

極超音速気流中において機体形状がエンジンに流入する気流に及ぼす影響について *

苅田丈士 *1、加藤周徳 *1、小寺正敏 *1、工藤賢司 *1、村上淳郎 *1、泉川宗男 *1、渡辺修一 *2

Abstract

The effect of the airframe configuration on the condition of the airflow to an engine was investigated experimentally in a hypersonic flow. Three kinds of forebody models of an aerospace plane were tested in the 1.27-m Mach 9.7 wind tunnel and in the 0.1-m Mach 6.7 pilot-wind tunnel. The leading edge of each model had a different width, that is, a pointed configuration, half of the body width, and the same width as the body. Pitot pressure was measured at the location of the engine entrance. The uniformity of the airflow to an engine was greatest in the model with the longest width at its leading edge. The airflow rate to the engine was large with large width of the leading edge of the airframe. This feature became significant in an engine with large height at the entrance. It was also made clear that the ratio of lift to drag was large in the model with a long leading edge, and that the influence of the shock wave – laminar boundary layer interaction did not spread laterally.

概　要

極超音速気流中において機体形状がエンジンに流入する気流に及ぼす影響について実験により検討を行なった。3 種類のスペースプレーンの機体模型を、1. 27 mマッハ 10 風洞と 0. 1 mマッハ 6. 7 風洞で実験した。3 種の機体模型の前縁幅を点状、機体の半分、そして機体と同じ幅とした。ピトー圧をエンジン入口位置で測定した。機体前縁幅が最大の模型で、エンジンに流入する気流の一様性は最大となった。エンジンに流入する気流流量も、機体前縁幅が最大の模型で最大となった。この流量特性はエンジン高さが高いほど顕著となった。揚力抗力比は機体前縁幅が長い模型で大きくなること、層流境界層と衝撃波との干渉の影響は流れを横断する方向へは広がらないことも明らかとなった。

---

*Received 31 July, 2007

*1 Combined Propulsion Research Group, Institute of Aerospace Technology（総合技術研究本部複合推進研究グループ）
*2 Foundation for Promotion of Japanese Aerospace Technology（財団法人 航空宇宙技術振興財団）

I. Introduction

Aerospace planes for a future transportation system to a low earth orbit are now under investigation. The scramjet engine and the combined cycle engine have been studied for Two-Stage-to-Orbit (TSTO) or Single-Stage-to-Orbit (SSTO) planes.[1,2] Figure 1 shows a schematic of an aerospace plane, the first stage of TSTO or SSTO. During flight in the supersonic and hypersonic regions, the windward surface of the vehicle pre-compresses air into the engine. The engine thrust is approximately proportional to the mass flow rate of the captured air.

Many kinds of airframe configurations of the aerospace plane have been reported.[3-5] Aerodynamic characteristics of the airframe have been investigated and the airflow into the engine has been examined.[6-9] However, the effect of the airframe configuration from the point of view of engine performance was not discussed.

The authors have previously shown the effect of the engine integration into the airframe on the engine performance[10] and the effect of the sides-spillage from the windward surface of the airframe on engine performance.[11] In the present study, another effect of the airframe on engine performance was examined, that is, the effect of the airframe configuration on the condition of airflow to an engine. The airframe configuration is related to aerodynamic stability and controllability. Herein, the focus is on the effect of the airframe on the engine performance. This effect was examined preliminary with inviscid CFD simulation.[12] In the present study, the effect was investigated with experiments conducted in hypersonic wind tunnels. Three typical airframe configurations were examined, that is, a pointed body shape, a rectangular shape, and a mixed shape. The airframe of the aerospace plane, as well as its wings, is an aerodynamic component. Herein, lift and drag of the three bodies by wall pressure integration are also presented.

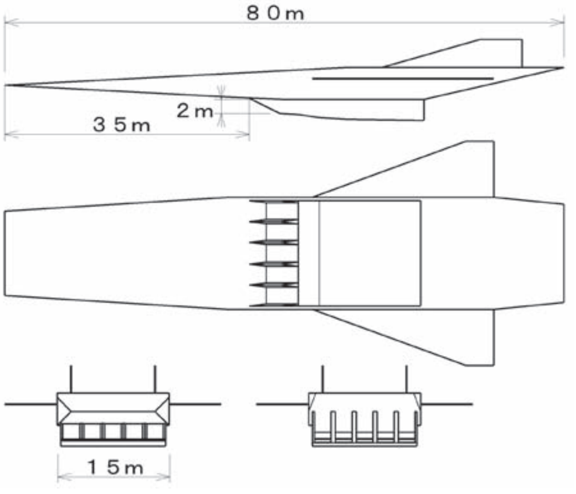

Fig. 1 Schematic of an aerospace plane.

Around the sides of the airframe with a swept-back side surface, as shown in Fig. 1, air flows into the engine through the side edge and the boundary layer grows a short distance from the edge to the engine. In the swept-back wings, the transition appears along the leading edge.[13] Transition of the boundary layer to a state of turbulence hardly spreads laterally. In an aerospace plane with swept-back sides, the boundary layer flows into the engine in the laminar condition.[14] The inflow of the laminar boundary layer easily induces separation due to interaction with the shock wave. In the present study, spread of a region affected by the shock wave - laminar boundary layer interaction was also examined.

II. Test Facility

Tests were conducted at the 1.27-m hypersonic wind tunnel (HWT) of the Wind Tunnel Technology Center and at the 0.1-m pilot wind tunnel (PWT) of the Combined Propulsion Research Group, Institute of Aerospace Technology, Japan Aerospace Exploration Agency (JAXA). Mach numbers of the wind tunnels were 9.7 of HWT and 6.7 of PWT. The total pressure, total temperature and exit diameter of HWT were 6.0 MPa, 1040 K and 1.27 m, respectively. The wall pressure at the exit of the facility nozzle was 1.69×10^{2} Pa. The Reynolds number was 3.6×10^{6} m^{-1}. The facility nozzle of PWT had a square cross section. The total pressure, the total temperature of the standard operating condition and the exit height of PWT were 6.0 MPa, 700 K, and 100 mm, respectively. The Reynolds number was 3.5×10^{7} m^{-1}.

III. Airframe Model Configuration

Test models and measurement of Mach 9.7 tests

Figure 2 shows the experimental models of the forward part of the aerospace plane airframe, from the leading edge to the engine entrance, used at the Mach 9.7 tests. Pitot pressure rakes were positioned at the engine entrance position. According to the conceptual study,[2] the plane will need an engine with such an entrance area to accelerate in the hypersonic flight regime. Under this configuration, the shock wave from the leading edge was designed to pass below the inlet at a flight Mach number of 12. The shock wave from the leading edge passes from a position of 2.2 m at the engine entrance in Fig. 1 at an angle of attack of 4 deg, that is, at a deflection angle of 8 deg from the airflow direction. In the experiments, the angle of attack, 0, 2, and 4 deg, was one parameter. Thus, the angles between the airflow and the windward surface of the models were 4, 6, and 8 deg, respectively. The thickness of the leading edge was 0.2 mm. The models were made of stainless steel.

The width of the leading edge of the models was another parameter. In model A, this width was the same as the width at the position where engine modules are to be attached. Model B had a leading edge of approximately half the width of the body. Model C had an approximately pointed airframe nose. The side surface of model C had a larger angle to the airflow than the windward surface. In the models, the imaginary engine entrance was located at 670 mm from the leading edge of the airframe on the windward surface.

The height of imaginary engine modules was 40 mm in the present models, and was expressed as *H*0. According to the two-dimensional shock wave relations, the shock wave from the leading edge was planned to pass 57 mm from the model surface at the angle of attack of 0 deg, and 53 mm at the angle of 4 deg. Pitot pressure was measured with Rake A and Rake B shown in Fig. 2 in the vertical direction at every 2.5 mm from the model surface to 20 mm and from 50 mm to 60 mm. Between 20 and 50 mm, the positions were every 5 mm. The measurement positions were 9 lateral positions

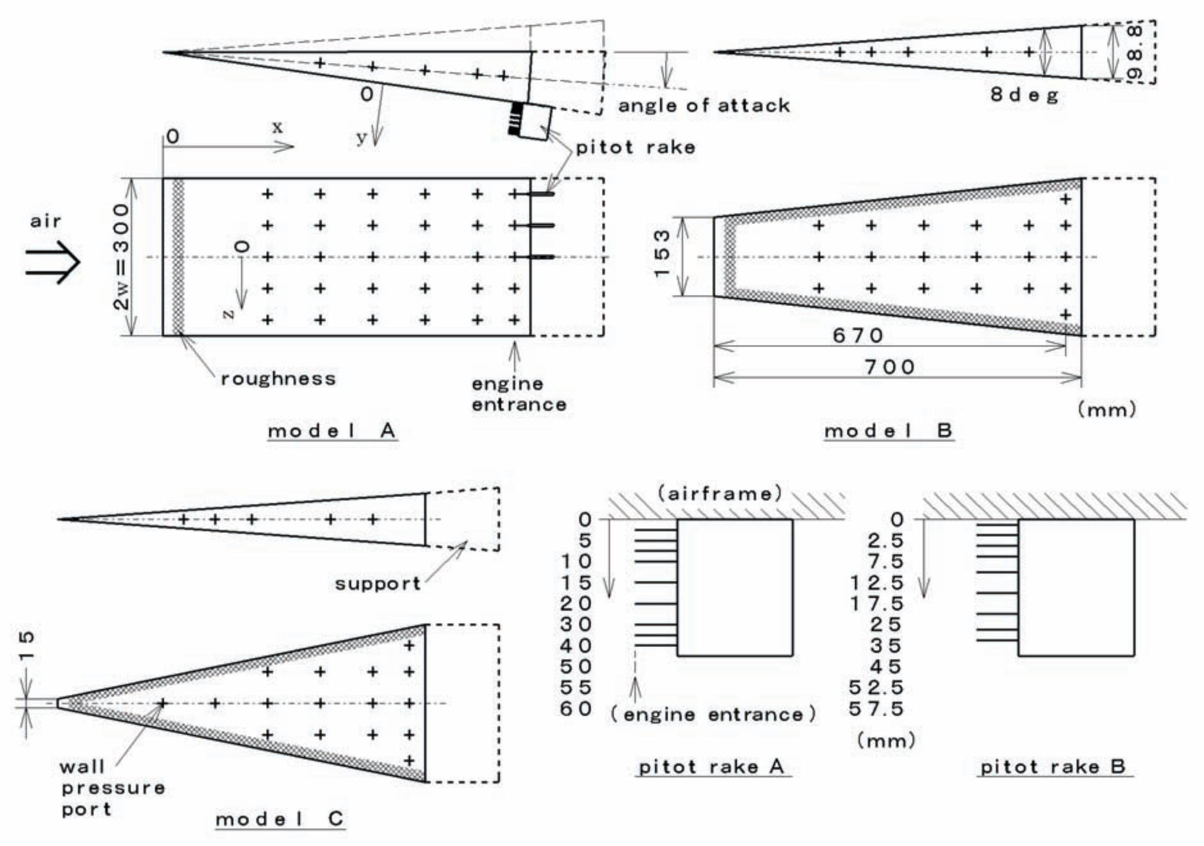

Fig. 2 Aerospace plane models and pitot rakes for Mach 9.7 tests. The shaded area denotes coating for roughness to change the boundary layer from laminar to turbulent.

from the center plane: 0 mm, -9 mm, -18 mm, -60 mm, -69 mm, -78 mm, -120 mm, -129 mm, and -138 mm. The pitot tubes were made of Inconel, their outer and inner diameters being 1 mm and 0.7 mm, respectively. The accuracy of the pitot pressure was 1.5 kPa.

Wall pressure of the airframe model was measured at the positions shown in Fig. 2 as intersections. On the leeward surface, wall pressure was measured at the same positions as on the windward surface. The positions were 30 on each surface and 5 on the side surface in model A. 20 on each surface and 5 on the side in mode B, and 16 on each surface and 5 on the side in model C. The accuracy of the wall pressure was 0.3×10^2 Pa, and the accuracy non-dimensionalized with the facility nozzle exit pressure was 0.18.

The Reynolds number in the actual flight will be 6.4×10^7 under the conditions of the reference length of 30 m from the leading edge to the engine and the flight dynamic pressure of 50 kPa. In the present tests, the Reynolds number was 2.4×10^6, being lower than the actual value. The models were coated with aluminum particles 500 to 600 μm in diameter for roughness between 20 mm and 50 mm from the leading edges of the models for transition of the boundary layer from laminar to turbulent. The coated areas are shaded in Fig. 2.

Test models and measurement of Mach 6.7 tests

Due to the smaller size of the wind tunnel, the models used in PWT shown in Fig. 3 were smaller but the same configuration as the models in Fig. 2. The models, the pitot rakes and the pitot tubes were made of stainless steel. The thickness of the leading edge of the models was 0.1 mm. In the Mach 6.7 tests, the model was fixed at the configuration of the angle of attack of 4 deg.

*H*0 was 8 mm in the Mach 6.7 tests, with the same proportion of the engine height to the airframe length. In Mach 6.7 flow, a shock wave calculated with the two-dimensional shock wave relation passed at 16 mm from the model surface, that is, 2*H*0 in non-dimensionalized form. The positions of the pitot rakes were z = 0 mm, -12 mm, and -24 mm, respectively, from the center plane. The positions of the probes were 2 mm, 5 mm, 8 mm, 11 mm, 14 mm, 17 and 20 mm from the model surface. The outer diameter and the inner

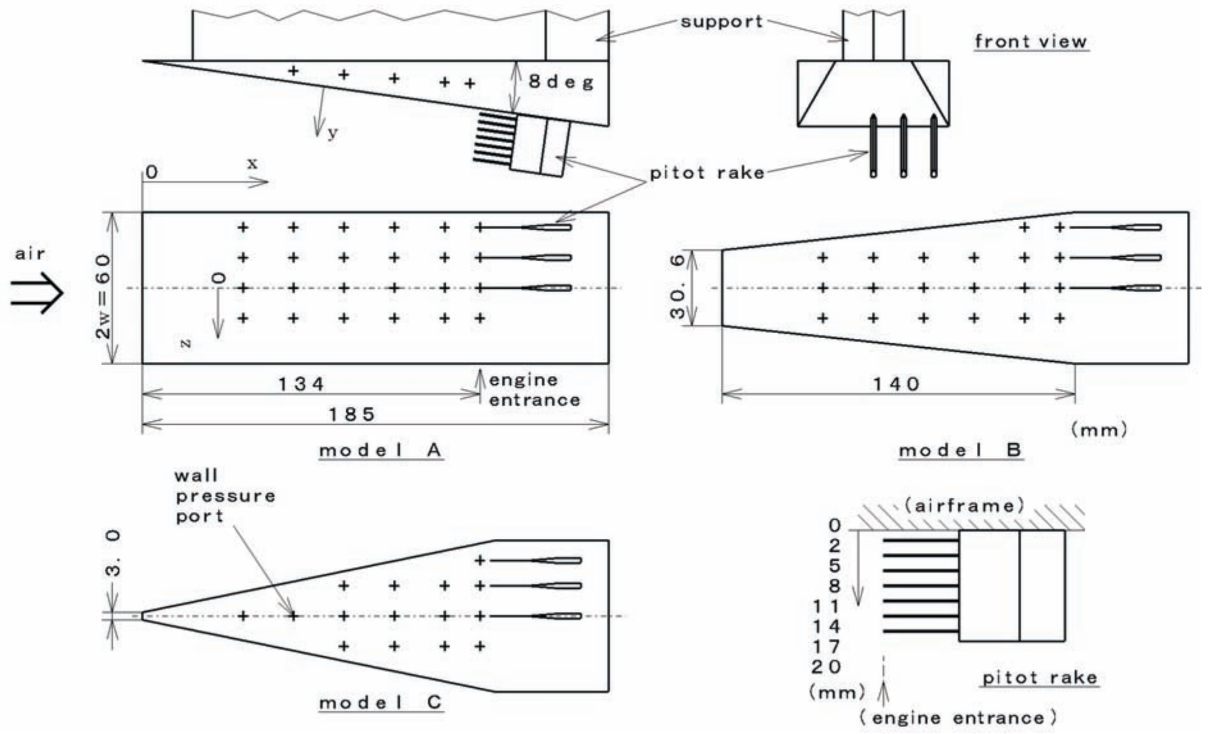

Fig. 3 Aerospace plane models and pitot rakes for Mach 6.7 tests. There was no wall pressure port on the leeward surface.

diameter of the tube were 0.6 mm and 0.3 mm, respectively. The accuracies of the wall pressure and the pitot pressure were 0.1 kPa, and the accuracy non-dimensionalized with the nozzle exit pressure was 0.06. The wall pressure of the leeward surface of the model was not measured. The wall pressure was measured at 24 positions on the windward surface and 5 positions on the side surface in model A. 20 on the windward surface and 5 on the side in model B, and 15 on the windward surface and 5 on the side in model C. The boundary layer was turbulent due to the large Reynolds number of PWT, and no coating for roughness was applied.

IV. Results and Discussion

Schlieren photo

Figure 4 shows schlieren photos of (a) model A and (b) model B at the angle of attack of 4 deg in the Mach 9.7 airflow of HWT. In Fig. 4(a), midway from the leading edge to the pitot rake, the boundary layer became thick. Transition from the laminar to the turbulent boundary layer took place here. According to other photos, the boundary layer transition was attained only at the 4 deg angle of attack with roughness, and no transition was attained at the other angles even with roughness. In both model B and model C, the transition also took place only at the 4 deg angle of attack with roughness. Fig. 4 (b) shows a picture of model B with no roughness. No transition took place.

Though the pitot probe had been designed to be higher than the shock wave from the leading edge, the shock wave from the model leading edge passed around the edge of the pitot rake, being far from the position calculated with the shock wave relation. This was caused by rapid growth of the boundary layer around the leading edge.

Pitot pressure distribution and shock wave location

(a) Mach 9.7 tests

Figure 5 shows pitot pressure distributions on the center plane ($z/w = 0$) and near the edge of the airframe ($z/w = -0.8$) at the angle of attack of 4 deg in the Mach 9.7 flow. w is the half width of the airframe body. The height of the probes from the model surface is non-dimensionalized by $H0$. As

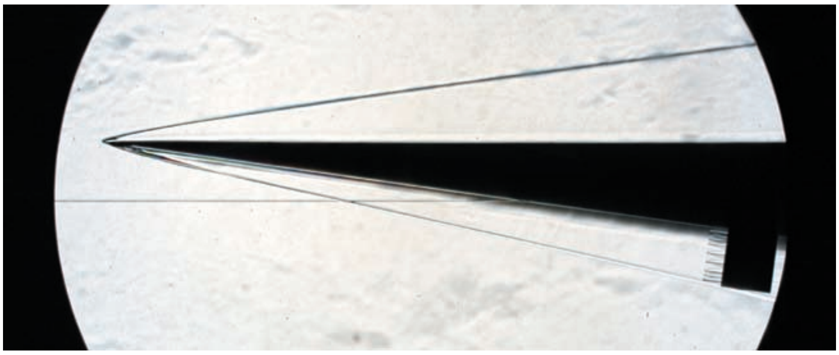
(a)

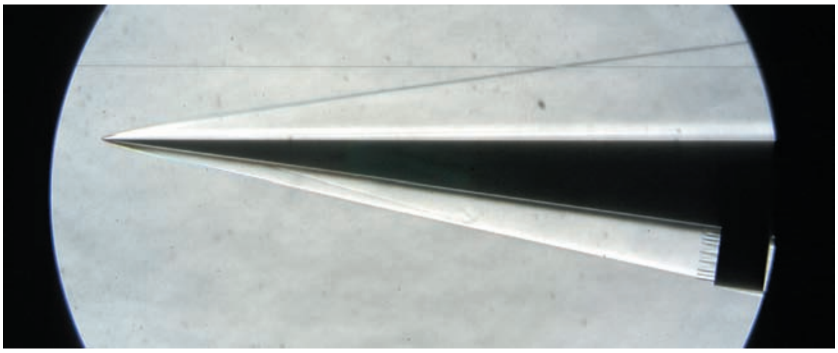
(b)

Fig. 4 Schlieren picture of airflow around a model at Mach 9.7 with angle of attack of 4 deg. (a) Roughness coated on model A. The boundary layer thickened midway between the leading edge and the pitot rake, indicating change from the laminar to the turbulent boundary layer. (b) No roughness coated on model B.

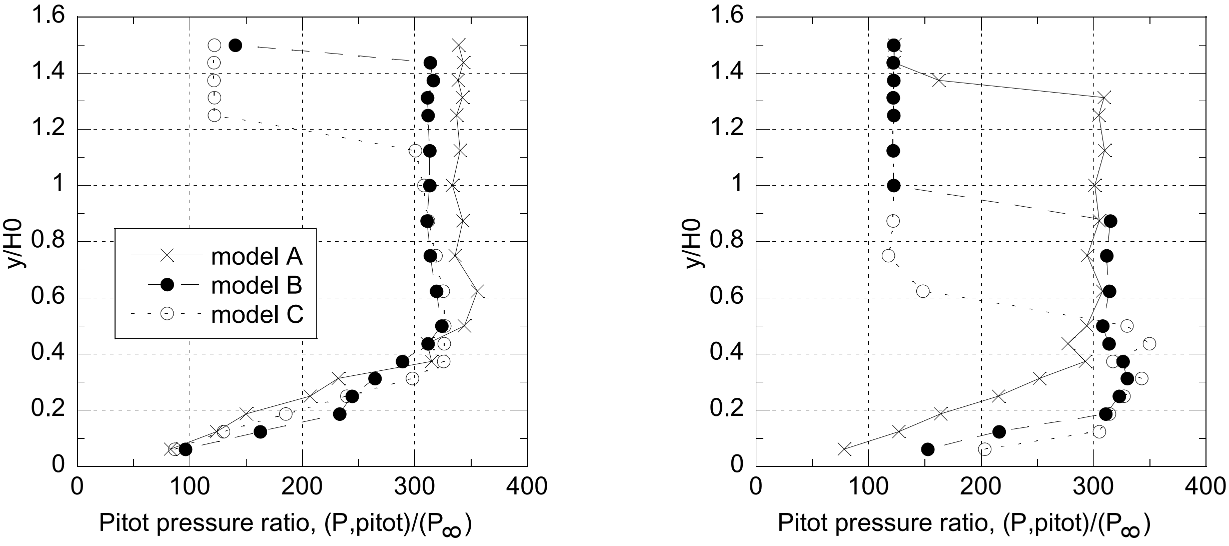

(a) z/W = 0. **(b) z/W = -0.8.**

Fig. 5 Pitot pressure distributions at the angle of attack of 4 deg in Mach 9.7 flow.

mentioned in the previous section, the shock wave from the model leading edge passed far from the model surface, and the highest tube was lower than the edge of the shock wave in the test using model A. The shock wave passed near the surface in model C. The shock wave was even closer to the surface at the edge of the airframe (*z*/*w* = -0.8).

The pitot pressure calculated with the shock wave relations is 330 behind the shock wave from the leading edge of the model in non-dimensionalized form, and 120 prior to the shock wave. The pitot pressures of the inviscid flow part of model A agreed with these pressures on the center plane, and the measured pressures were lower at *z*/*w* = -0.8.

In models B and C, the pitot pressures of the inviscid flow part were lower than those of model A on the center plane. On the other hand, the pressures of models B and C on the center plane were almost the same as those at *z*/*w* = -0.8. In these two models, the pressure on the side surface was similar to or higher than that on the windward surface due to the large deflection angle of the side surface. The influence of expansion fans from the corners on spillages from the windward surface to the sides was suppressed. This resulted in suppression of an increase of the Mach number, and the pitot pressures at *z*/*w* = -0.8 became high.

In models B and C, the heights of the boundary layer were almost the same as the height in model A on the center plane, but were smaller than that in model A at *z*/*w* = -0.8. In models B and C, the length from the side leading edge to the engine entrance was short at *z*/*w* = -0.8, and the boundary layers were thin. At *z*/*w* = -0.8, the boundary layer might be laminar in the models B and C, and the shock wave from the pitot probe tube might induce separation of the boundary layer. According to the pitot pressure distributions, significant changes of the airflow field were not induced as shown later even though there might be interaction between the shock wave and the boundary layer.

Figure 6 shows the location of the shock waves judged from the change of the pitot pressure. In the figure, *H*1 is 1.25 times and *H*2 is 1.5 times as high as *H*0, respectively. *H*1 is 50 mm and *H*2 is 60 mm from the model surface. As the width of the leading edge of the airframe became short, the shock wave passed near the model surface, especially around the sides of the airframe models. The distributions showed that the large width of the leading edge was favorable for pre-compression. The uniformity of airflow flowing to an engine was largest in model A with the greatest leading edge width.

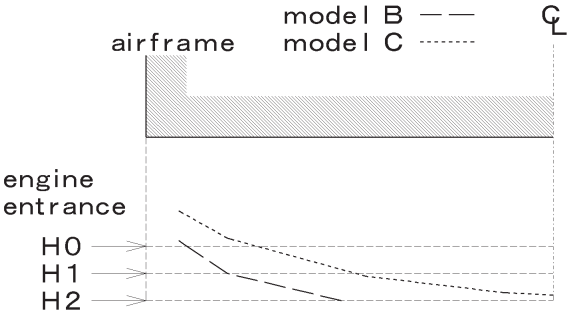
model B
model C
airframe
CL
engine entrance
H0
H1
H2

(a) Attack angle was 0 deg.

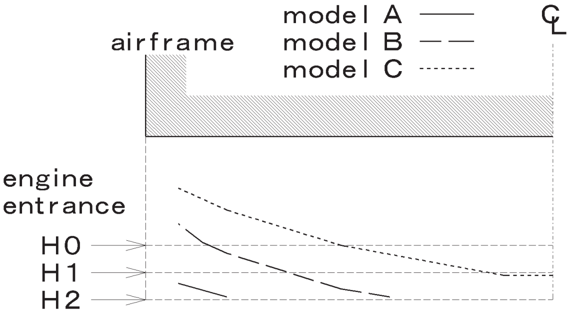
model A
model B
model C
airframe
CL
engine entrance
H0
H1
H2

(b) Attack angle was 2 deg.

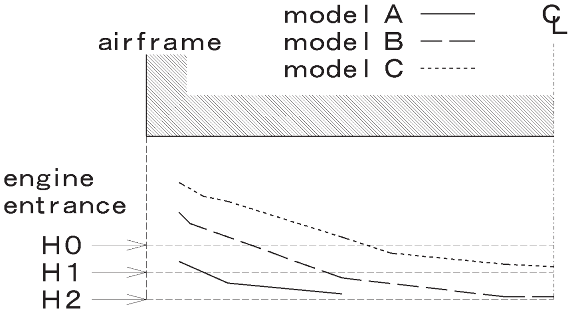
model A
model B
model C
airframe
CL
engine entrance
H0
H1
H2

(c) Attack angle was 4 deg.

Fig. 6 Locations of shock wave from leading edge in Mach 9.7 flow, based on pitot pressure measurement.

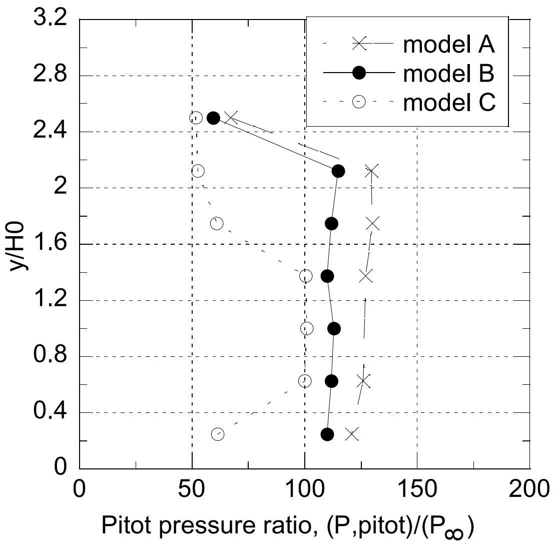

(a) z/W = 0.

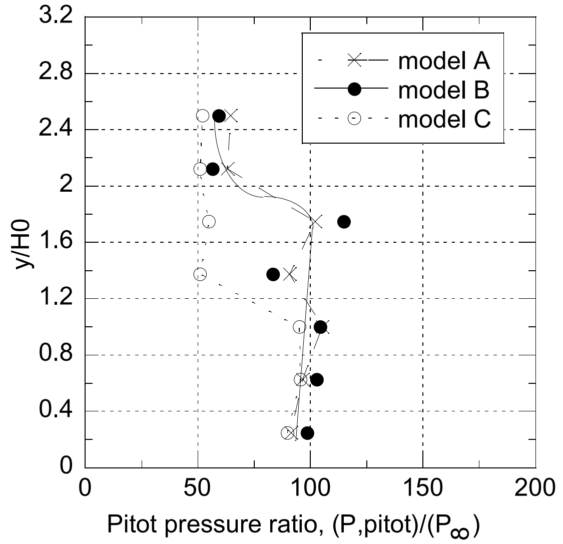

(b) z/W = -0.8.

Fig. 7 Pitot pressure distributions at the angle of attack of 4 deg in Mach 6.7 flow.

(b) Mach 6.7 tests

Figure 7 shows pitot pressure distributions in the Mach 6.7 flow on the center plane ($z/w = 0$) and near the edge of the airframe ($z/w = -0.8$). In the Mach 6.7 condition, calculated pitot pressures are 120 behind the shock wave from the leading edge, and 58 prior to the shock.

In models A and B, the boundary layer was not thick and could not be measured by the probes. On the center plane of model C, there was a low pitot pressure region on the wall. This indicates the possibility of a secondary flow from the side surface to the windward surface. In model C, the non-dimensionalized pressure was 3.6 on the sides and higher than the pressure on the windward surface of 2.9. This higher pressure probably induced a secondary vortex flow on the windward surface.

On the center plane, the level of the pitot pressure downstream of the shock wave was lower in model B than model A, as was also the case in the Mach 9.7 flow. The level of model C was further lower than that of model B. At $z/w = -0.8$, there was no difference in the pitot pressure behind

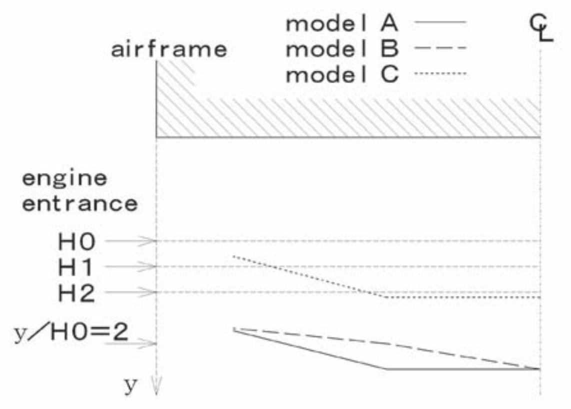

Fig. 8 Locations of shock wave from leading edge in Mach 6.7 flow, based on pitot pressure measurement.

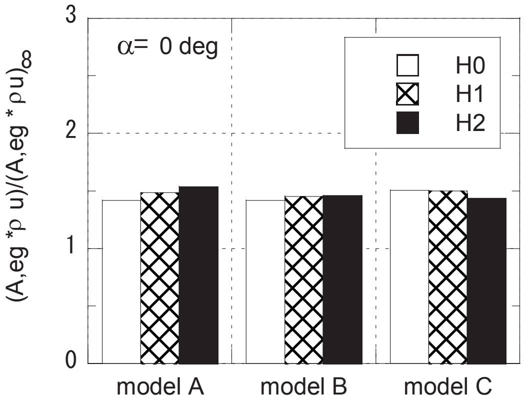

(a) Angle of attack was 0 deg.

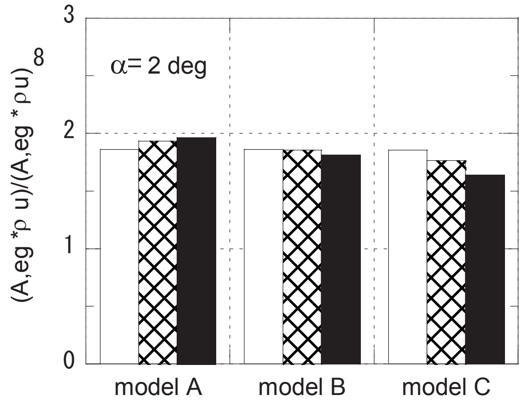

(b) Angle of attack was 2 deg.

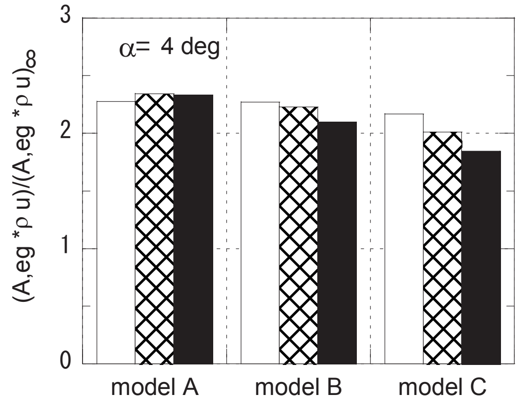

(c) Angle of attack was 4 deg.

Fig. 9 Rate of airflow into the engine in Mach 9.7 flow.

the shock wave in the core flow, and the pressure of model C at *z/w* = -0.8 was almost the same as that on the center plane.

Figure 8 shows the location of the shock waves. The shock waves were located farther from the wall than the waves in the Mach 9.7 flow. Among the shock waves in the Mach 6.7 flow, the wave of model C was located nearest the wall, as was also the case in the Mach 9.7 flow. Between models A and B, there was no significant difference in the shock wave location.

Airflow rates

Rates of airflow to the engine were calculated with the pitot pressure measured at the imaginary model position. The wall pressure was used in place of static pressure. Figures 9 (a) to (c) show the rates of airflow of the three airframe models in the Mach 9.7 flow. The rates were non-dimensionalized with mass flux of the core flow of the wind tunnel (ρu_∞) and the projected area at the imaginary engine entrance (*A,eg*). For example, the airflow rate measured in the area with the height of *H*2 is non-dimensionalized with the height of *H*2.

The impulse function, *I*, is expressed as below.

$$I = \dot{m}u + PA \qquad (1)$$

$\dot{m}$ is mass flow rate, *u* is velocity, *P* is static pressure and *A* is cross section. In the hypersonic regime, momentum makes a larger contribution to the impulse function than pressure. The velocity does not change greatly in the region of a weak shock wave. Therefore, the non-dimensionalized impulse function into the engine is almost proportional to the non-dimensionalized mass flow rate. Thus, the figures of the impulse function are not shown here.

At the 0 deg angle of attack, there was no significant difference or change in the non-dimensionalized airflow rate between the models nor between the heights of the engine. As shown in Fig. 6, the shock waves were located far from the model surface in the three models, so no significant difference appeared.

As the height of the engine increases from *H*0 to *H*2, the ratio of the boundary layer decreases, whereas the ratio of the airflow rate without pre-compression increases. The decrease of the non-dimensionalized flow rate with the increase of the engine height was significant in models B and C at the 4 deg angle of attack. In the models, the shock waves passed closer to the model surface than in model A as shown in Fig. 6(c), and the ratio of the non-pre-compressed airflow rate increased with the increase of the engine height. This influenced greater than the decrease of the ratio of the boundary layer on the rate of airflow into an engine. The rate was large in the model with a long leading edge.

Figure 10 shows the non-dimensionalized rate of airflow to an engine in the three airframe models in the Mach 6.7 flow. The flow rates were smaller than those in the Mach 9.7 flow, though the shock waves passed far from the model surface. This was caused by a lower pre-compression in the Mach 6.7 flow. The airflow rate was lower in model C than in models A and B, i.e., the airflow rate became small as the length of the leading edge became short, as was the case in the Mach 9.7 flow.

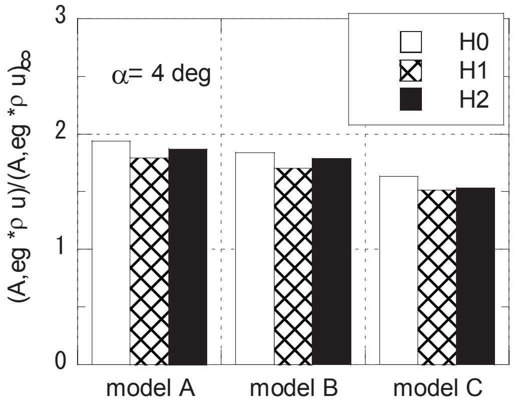

Fig. 10 Rate of airflow into the engine in Mach 6.7 flow.

From the results in the Mach 9.7 flow and the Mach 6.7 flow, the configuration with a longer leading edge such as in model A was preferable for the mass flow rate to an engine. When an engine is large such as those whose height is *H*2, the difference in the mass capture becomes clearer. Even when an engine is small such as those whose height is *H*0, the difference is still clear for a lower Mach number, as shown by the result of the Mach 6.7 flow condition.

Pressure distribution on windward and leeward surfaces

(a) Mach 9.7 tests

Figures 11 to 13 show isobars on the windward surface and Figures 14 to 16 show those on the

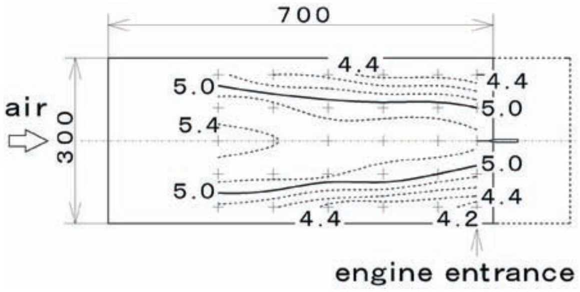

(a) Model A.

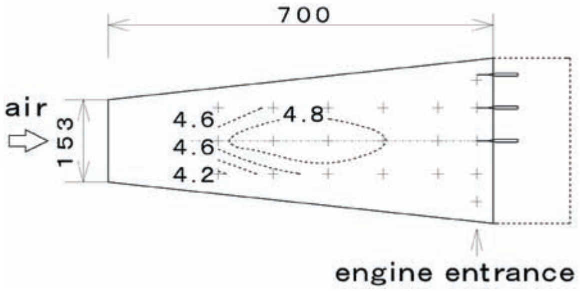

(b) Model B.

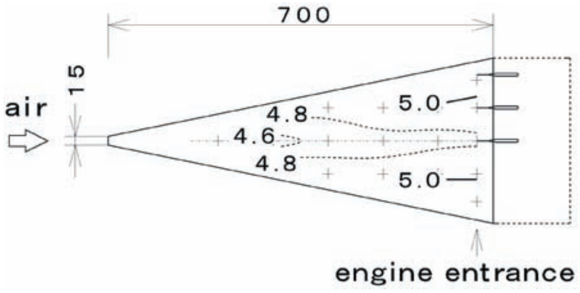

(c) Model C.

Fig. 11 Isobars on windward surface at angle of attack of 4 deg in Mach 9.7 flow.

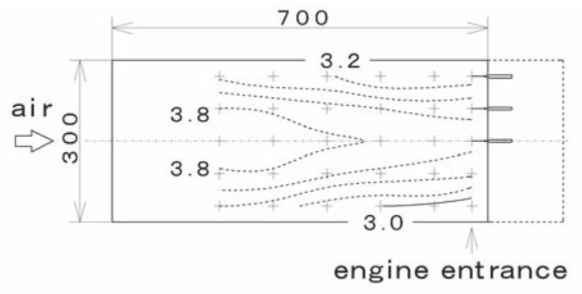

(a) Model A.

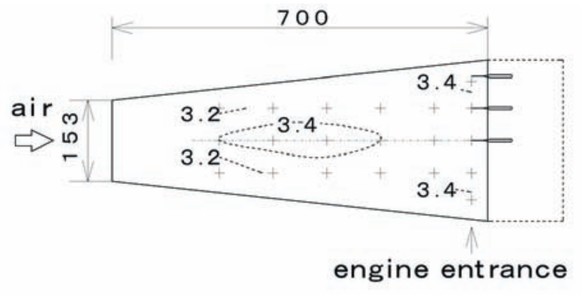

(b) Model B.

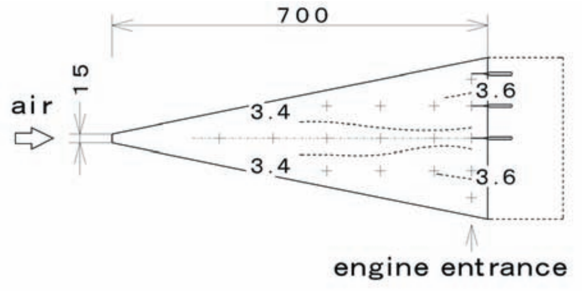

(c) Model C.

Fig. 12 Isobars on windward surface at angle of attack of 2 deg in Mach 9.7 flow.

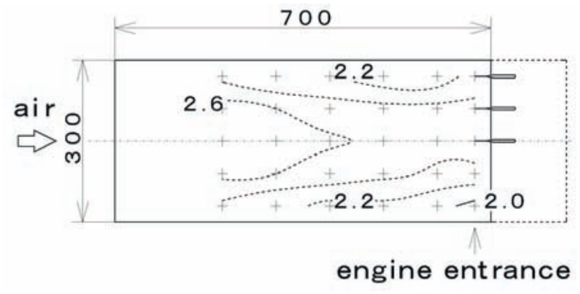

(a) Model A.

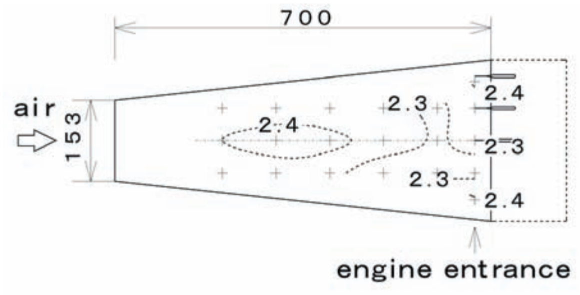

(b) Model B.

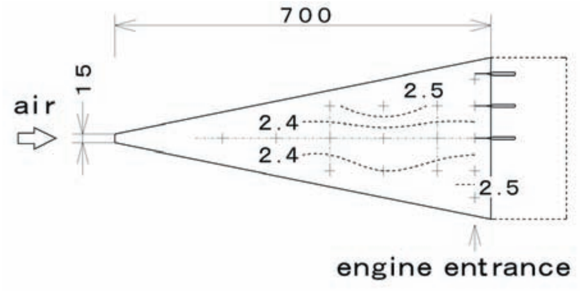

(c) Model C.

Fig. 13 Isobars on windward surface at angle of attack of 0 deg in Mach 9.7 flow.

leeward surface of the models in the Mach 9.7 flow. At the angle of attack of 0 deg, the deflection angle of the windward surface is the same as that of the leeward surface.

On the windward surface, spreading of expansion waves was clear in the isobars of model A. However, the pressure level was still high in model A, which had the largest two-dimensionality of the three models at the imaginary engine entrance position. In the model B, pressure was approximately uniform at all the angles of attack. In the model C, pressure near the side leading edges was higher than that on the center due to the large deflection angle of the sides of model C.

On the leeward surface at the angle of attack of 4 deg, the pressure distributions were approximately uniform due to no deflection angle of the surface from the airflow direction.

(b) Mach 6.7 tests

In the Mach 6.7 tests, wall pressure was measured only on the windward surface at the angle of attack of 4 deg. Spreading of expansion waves was clear in the isobars and the pressure level was high in model A, as was the case in the Mach 9.7 flow. In model C, no large pressure distribution was measured, differing from the distribution in the Mach 9.7 tests.

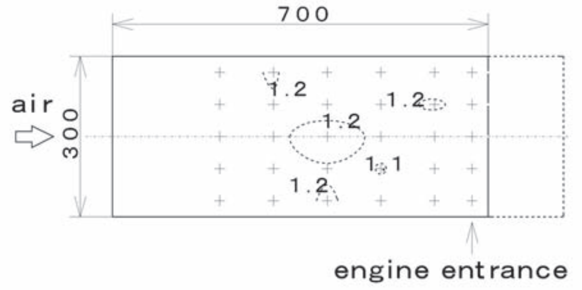
700
air
300
1.2
1.2
1.2
1.1
1.2
engine entrance

(a) Model A.

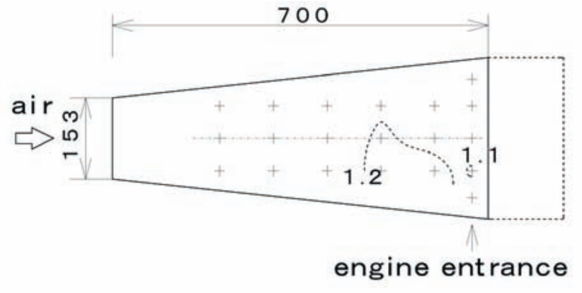
700
air
153
1.2
1.1
engine entrance

(b) Model B.

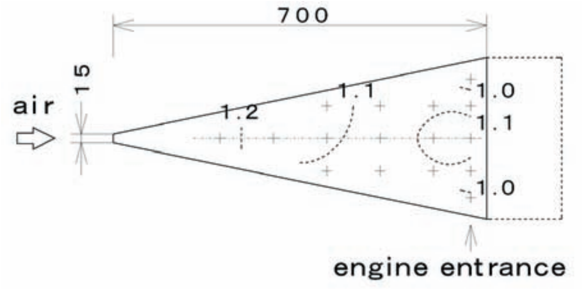
700
air
15
1.2
1.1
1.0
1.1
1.0
engine entrance

(c) Model C.

Fig. 14 Isobars on leeward surface at angle of attack of 4 deg in Mach 9.7 flow.

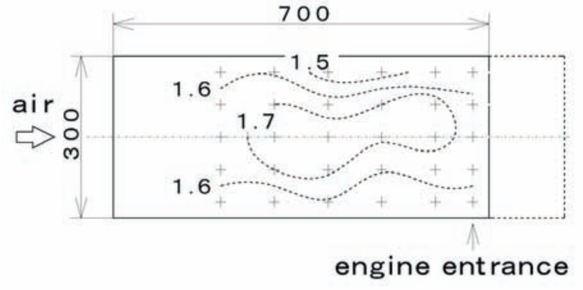
700
air
300
1.5
1.6
1.7
1.6
engine entrance

(a) Model A.

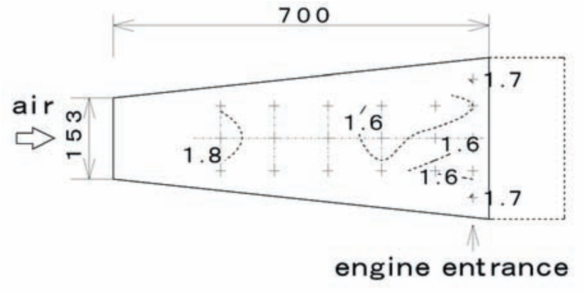
700
air
153
1.7
1.6
1.8
1.6
1.6
1.7
engine entrance

(b) Model B.

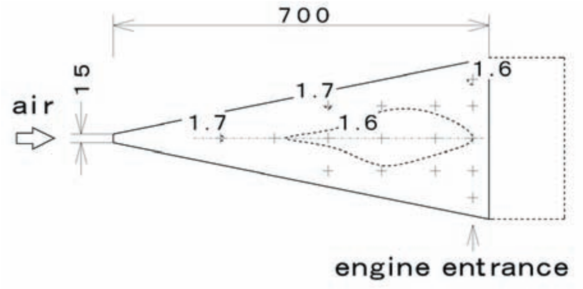
700
air
15
1.6
1.7
1.7
1.6
engine entrance

(c) Model C.

Fig. 15 Isobars on leeward surface at angle of attack of 2 deg in Mach 9.7 flow.

Pressure drag and lift of the models

By integrating the wall pressure on the model surface, approximate pressure drag and lift of the models could be estimated. This included the force on the windward and leeward surfaces of the model from the leading edge to the entrance of the imaginary engine position, but did not include the drag/force on the support section and the base area. Figure 18 shows pressure drags, and Fig. 19 shows ratios of lift to drag, *L*/*D*, in the Mach 9.7 flow. The drag was non-dimensionalized with the cross section of the airframe model at the engine entrance position, (A,*cross*), and the dynamic pressure of the inflow air (q_∞). The accuracy of the non-dimensionalized drag was 0.003. The slight *L*/*D* at the angle of attack of 0 deg was due the errors of the wall pressure measurement and the model configurations. *L*/*D* of model A with a rectangular projected area was similar to a previous result.[15]

The pressure on the side surface remained approximately constant at all three angles of attack. In model B, the pressure on the side surface was 3. At the 0 deg angle of attack, the pressure on the windward surface was 2.4, and the pressure on the side surface was higher than the pressure on the windward surface. Therefore, the drag of model B was slightly larger than that of model A. At the 4 deg angle of attack, the pressure on the windward surface was 4.7 and the pressure on the side was lower than the pressure on the windward surface.

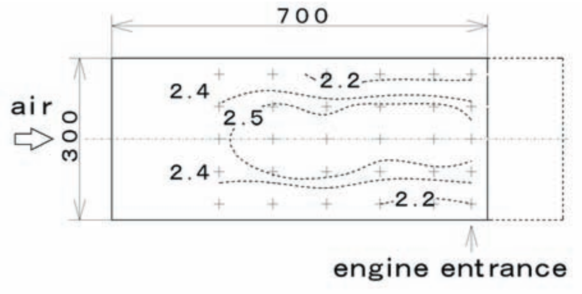
700
air
300
2.4
2.2
2.5
2.4
2.2
engine entrance

(a) Model A.

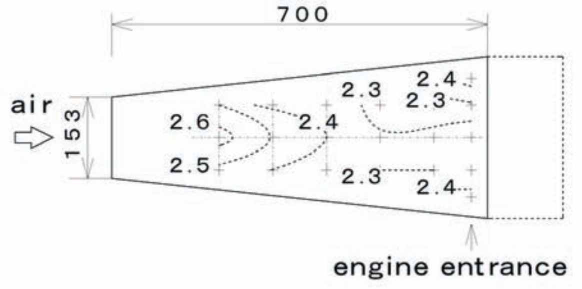
700
air
153
2.3
2.4
2.3
2.6
2.4
2.5
2.3
2.4
engine entrance

(b) Model B.

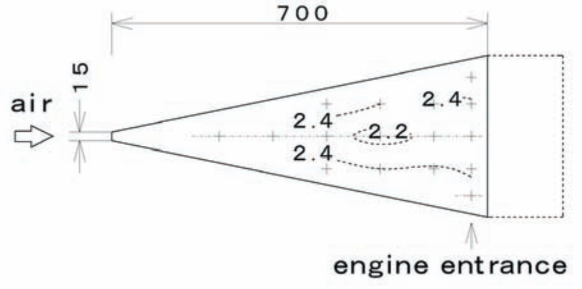
700
air
15
2.4
2.4
2.2
2.4
engine entrance

(c) Model C.

Fig. 16 Isobars on leeward surface at angle of attack of 0 deg in Mach 9.7 flow.

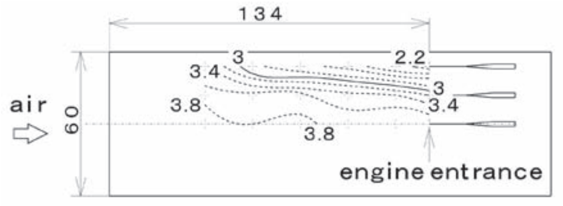
134
air
60
3
2.2
3.4
3
3.8
3.4
3.8
engine entrance

(a) Model A.

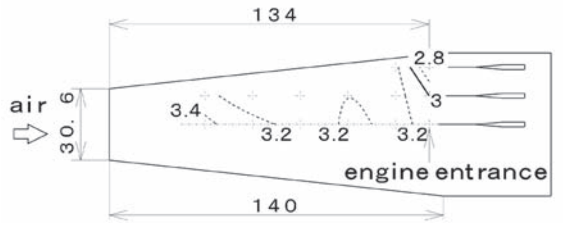
134
2.8
air
30.6
3.4
3
3.2
3.2
3.2
engine entrance
140

(b) Model B.

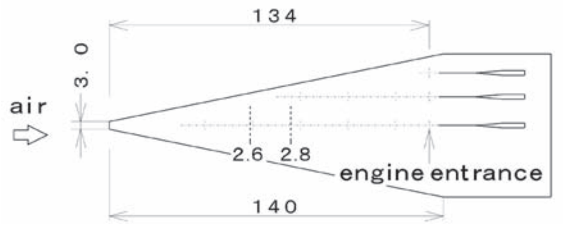
134
3.0
air
2.6
2.8
engine entrance
140

(c) Model C.

Fig. 17 Isobars on windward surface at angle of attack of 4 deg in Mach 6.7 flow.

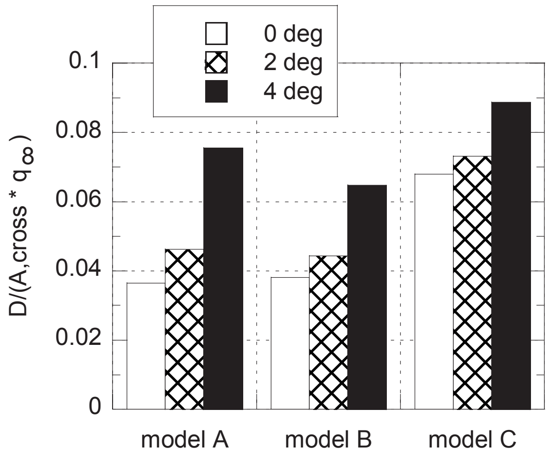

Fig. 18 Non-dimensionalized pressure drag in Mach 9.7 flow.

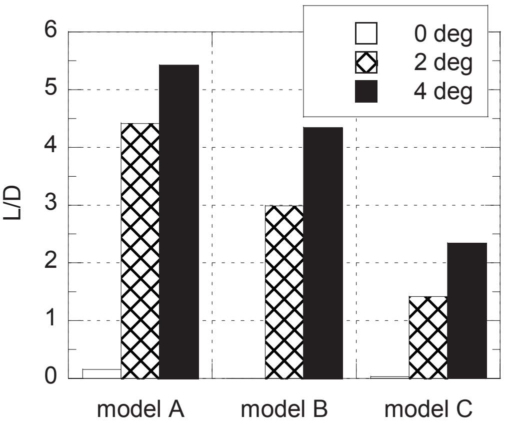

Fig. 19 L/D in Mach 9.7 flow.

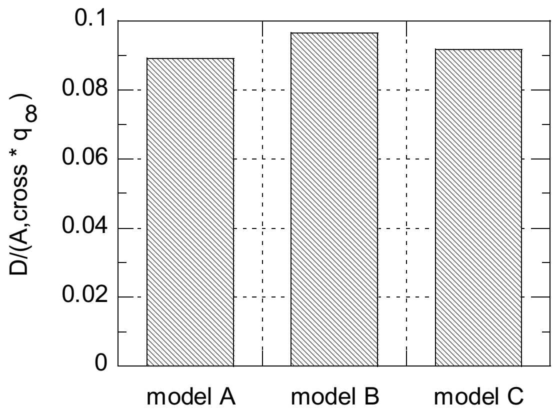

Fig. 20 Pressure drag in Mach 6.7 flow.

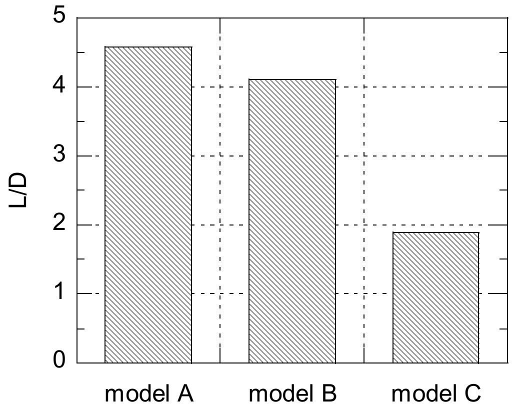

Fig. 21 L/D in Mach 6.7 flow.

Therefore, the drag of model B became smaller than that of model A. In model C, the side surface had a larger angle to the airflow than the windward surface, and the pressure on the sides, which was 7, was higher than the pressure on the windward surface at all three angles of attack. Therefore, the drag of model C was largest in the models.

L/*D*'s were higher in models A and B than in model C. The lift of model A was approximately 1.5 times as high as that of model B. The lift of model B was also approximately 1.5 times as high as that of model C. In model C, as shown in Fig. 18, the drag was larger than those of the other two models. The difference in the *L*/*D*'s was caused by these differences in lift and drag.

Figure 20 shows pressure drags, and Figure 21 shows *L*/*D*'s in the Mach 6.7 flow. The pressure on the leeward surface was presumed to be the same as that of the inflow air due to the fact that the deflection angle of the leeward surface was 0 deg. The accuracy of the non-dimensionalized drag was 0.002.

In contrast to the result in the Mach 9.7 flow, the drag of model C was not larger than those of the other two models. This was due to the fact that the pressure level on the windward surface was lower in model C than in models A and B, as shown in Fig. 17, though the pressure level on sides was higher. However, *L*/*D* decreased with the decrease of the width of the leading edge. The difference of lift was larger than that of drag. The *L*/*D*'s of the models resembled those in the Mach 9.7 flow, respectively.

Lateral spread of shock wave - laminar boundary layer interaction

The spread of the shock wave - laminar boundary layer interaction was investigated with the change of wall pressure measured at the imaginary engine entrance position caused by the pitot rakes or their tubes in Mach 9.7 flow. The pitot rake A's were attached at z/w = 0, -0.4, and -0.8. The pitot tube of the rake closest to the wall was located at y = 5 mm. The rakes or the tubes would induce the interaction between the shock wave and the boundary layer. On half of the airframe, there was no pitot rake. The angle of attack was 4 deg. With roughness, the boundary layer was turbulent at the engine entrance at this angle and was laminar with no roughness. The accuracy of the non- dimensionalized pressure was 0.18.

Figures 22 (a) to (c) show the wall pressure distributions with or without roughness. In model A, the pressure on the sides was lower than that on the windward surface, and the pressure became low toward the sides on the windward surface due to the expansion fan. In model C, the pressure on the sides was higher than that on the windward surface, so the pressure became high toward the sides.

Pressure distribution was asymmetrical with no roughness condition in the models. The influence of the pitot rakes did not spread to the region without a rake. In model C, the pressure at z/w =

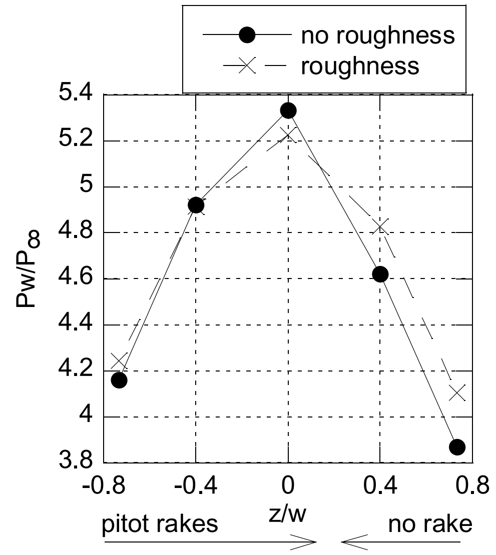

(a) Model A.

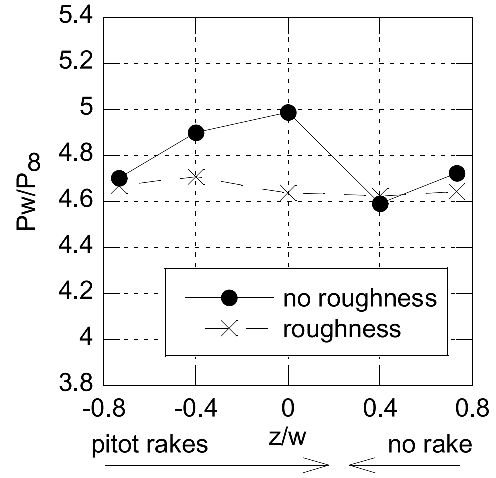

(b) Model B.

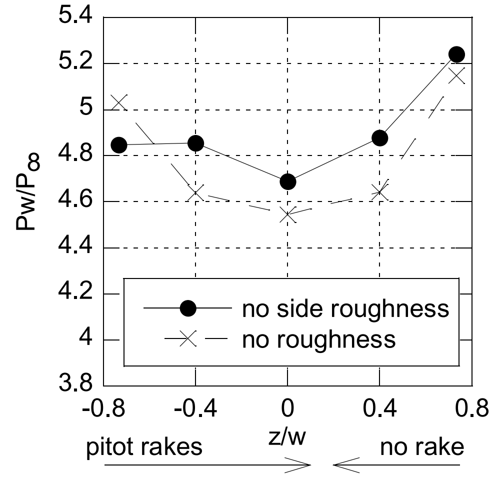

(c) Model C.

Fig. 22 Wall pressure under laminar boundary layer condition at engine entrance.

-0.8 became low and the pressure distribution also became asymmetrical. The change appeared only at *z*/*w* = -0.8 and did not spread laterally.

Under the inflow of the laminar boundary layer, the interaction between the shock wave and the boundary layer appeared by the pitot rakes located downstream. The inflow boundary layer should be turbulent, and the airframe with side leading edges should have devices for boundary transition.[16]

V. Conclusions

The effect of the airframe configuration on the condition of airflow to the engine was investigated with three kinds of forebody models in Mach 9.7 and Mach 6.7 flows experimentally. The present study clarified the following points.

(1) The uniformity of airflow to an engine was greatest in model A with the longest width at its leading edge.

(2) The airflow rate to the engine was large with large width of the leading edge of the airframe. This feature became significant in an engine with large height at the entrance.

(3) The ratio of lift to drag was large in the model with a long leading edge.

(4) The influence of the shock wave - laminar boundary layer interaction did not spread laterally.

Acknowledgements

The authors appreciate the kindness of Dr. A. Murakami and Dr. Y. Watanabe of JAXA, and Mr. T. Yamaji, a graduate student of Tokyo University of Science and currently a research engineer of Mitsubishi Heavy Industry, Ltd., for acquisition of pressure data. The authors also wish to thank the staff of the Hypersonic Wind Tunnel Section of JAXA for conducting the experiments.

References

[1] Chinzei, N., “Research Activities on Scramjets at NAL-KRC in Japan,” 15th International Symposium on Air-Breathing Engines Paper, ISABE-2001-1075, AIAA, Reston, VA, Sep. 2001.

[2] Kanda, T., and Kudo, K., “Conceptual Study of a Combined-Cycle Engine for an Aerospace Plane,”

Journal of Propulsion and Power, Vol. 19, No. 5, 2003, pp. 859-867.

[3]Boger, T. J., Alberico, J. F., Johnson, D. B., Espinosa, A. M., and Lockwood, M. K., "Dual-Fuel Lifting Body Configuration Development," AIAA Paper 96-4592, Nov. 1996.

[4]Weinreich, H.-L., Grallert, H., Parkinson, R., and Berry, W., "Studies on a Scramjet-propelled, Horizontal Launch and Landing, Single-Stage-to-Orbit Launcher," AIAA Paper 93-5053, Nov. 1993.

[5]Lockwood, M. K., Petley, D. H., Martin, J. G., and Hunt, J. L., "Airbreathing Hypersonic Vehicle Design and Analysis Methods and Interactions," *Progress in Aerospace Sciences*, Vol. 35, 1999, pp. 1-32.

[6]Ide, H., Armstrong, J., Szema, K. Y., and Haney, J., "Hypersonic Vehicle Forebody Design Studies," AIAA Paper 89-2182-CP, 1989.

[7]Berens, T. M., and Bissinger, N. C., "Forebody Precompression Effects and Inlet Entry Conditions for Hypersonic Vehicles," *Journal of Spacecraft and Rockets*, Vol. 35, No. 1, 1998, pp. 30-36.

[8]Bertin, J. J., Towne, M. C., Malan, M. A., Kreins, A. F., Zuber, M. E., and Parks, M. B., Viscous/Inviscid Interactions of the Forebody Flowfield of an Airbreathing Hypersonic Vehicle," *Journal of Spacecraft and Rockets*, Vol. 35, No. 4, 1998, pp. 442-449.

[9]Goonko, Y. P., and Mazhul, I. I., "Some Factors of Hypersonic Inlet/Airplane Interactions," *Journal of Aircraft*, Vol. 39, No. 1, 2002, pp. 37-50.

[10]Akihisa, D., Kanda, T., Tani, K., Kudo, K., and Masuya, G., "Effect of Integration of Scramjet into Airframe on Engine Performance and Payload," *Journal of Propulsion and Power*, Vol. 18, No. 5, 2002, pp. 1026-1032.

[11]Tani, K., Kanda, T., Kudo, K., and Akihisa, D., "Effect of Sides-Spillage from Airframe on Scramjet Engine Performance," *Journal of Propulsion and Power*, Vol. 17, No. 1, 2001, pp. 139-145.

[12]Kodera, M., Kanda, T., Tani, K., "Effect of Airframe Geometry on Thrust Performance of Aerospace Plane," AIAA Paper 2000-3342, Jul. 2000.

[13]Hozumi, K., Nomura, S., Aihara, Y., Morishita, E., and Okunuki, T., "Experimental Investigation of Aerothermal Problems Associated with Hypersonic Flight of HST," *Proceedings of 18th Congress of the International Council of the Aeronautical Sciences*, ICAS and AIAA, Reston, VA, Sep. 1992, pp. 1863-1875.

[14]Private communication with Dr. Shinji Nagai, Senior researcher of JAXA.

[15]Hankey, W. L., and Elliott, G. A., "Hypersonic Lifting Body Optimization," *Journal of Spacecraft and Rockets*, Vol. 5, No. 12, 1968, pp. 1463-1467.

[16]Berry, S. A., Auslender, A. H., Dilley, A. D., and Calleja, J. F., "Hypersonic Boundary-Layer Trip Development for Hyper-X," *Journal of Spacecraft and Rockets*, Vol. 38, No. 6, 2001, pp. 853-864.

JAXA Research and Development Report JAXA-RR-07-007E

Date of Issue : December 28, 2007
Edited and Published by : Japan Aerospace Exploration Agency
7-44-1 Jindaiji-higashimachi, Chofu-shi, Tokyo 182-8522 Japan
URL : http://www.jaxa.jp/
Printed by : Kokyusha

Inquires about copyright and reproduction should be addressed to the Aerospace Information Archive Center, Information Systems Department, JAXA.

2-1-1 Sengen, Tsukuba-shi, Ibaraki 305-8505, Japan
phone : +81-29-868-5000 fax : +81-29-868-2956

Copyright © 2007 by JAXA.
All rights reserved. No part of this publication may be reproduced, stored in retrieval system or transmitted, in any form or by any means, electronic, mechanical, photocopying, recording, or otherwise, without permission in writing form the publisher.

Japan Aerospace
Exploration Agency

Printed on Recycled Paper